

Theory of atomic-scale dielectric permittivity at insulator interfaces

Feliciano Giustino and Alfredo Pasquarello

*Ecole Polytechnique Fédérale de Lausanne (EPFL), Institute of Theoretical Physics, CH-1015 Lausanne, Switzerland
and Institut Romand de Recherche Numérique en Physique des Matériaux (IRRMA), CH-1015 Lausanne, Switzerland*

(Received 7 July 2004; revised manuscript received 10 December 2004; published 8 April 2005)

We develop a theory for investigating atomic-scale dielectric permittivity profiles across interfaces between insulators. A local susceptibility $\chi(x; \omega)$ is introduced to describe variations of the dielectric response over length scales of the order of interatomic distances. The nonlocality of the microscopic susceptibility tensor $\chi_{ij}(\mathbf{r}, \mathbf{r}'; \omega)$ occurs at smaller distances and therefore does not intervene in our formulation. The local permittivity is obtained from the microscopic charge density induced by an applied electric field. We show that the permittivity can conveniently be analyzed in terms of maximally localized Wannier functions. In this way, we can relate variations of the microscopic dielectric response to specific features of the local bonding arrangement. In addition to a continuous description in terms of the local permittivity, we introduce an alternative scheme based on discrete polarizabilities. In the latter case, electronic polarizabilities $\alpha_{\text{elec}}^{(n)}$ are obtained in terms of the displacements of maximally localized Wannier functions, while ionic polarizabilities $\alpha_{\text{ion}}^{(l)}$ are determined from the induced ionic displacements and the corresponding dynamical charges. The potential of our scheme is illustrated through applications to two systems of technological interest. First, we consider the permittivity of Si slabs of finite thickness. Our approach indicates that the local permittivity in the slab interior approaches the corresponding value for bulk Si within a few atomic layers from the surface. Therefore, the decrease of the average slab permittivity with thickness originates from the lower permittivity of the outer planes and the increasing surface-to-volume ratio. Second, we address the dielectric permittivity across the Si(100)-SiO₂ interface. Using two distinct interface models, we are able to show that the dielectric transition from the silicon to the oxide occurs within a width of only a few Å. The polarizability associated to intermediate oxidation states of Si is found to be enhanced with respect to bulk SiO₂, resulting in a larger permittivity of the interfacial suboxide layer with respect to the stoichiometric oxide.

DOI: 10.1103/PhysRevB.71.144104

PACS number(s): 77.55.+f, 73.61.-r, 73.20.-r, 71.15.Mb

I. INTRODUCTION

Current technological developments drive the growing request for the characterization of the dielectric properties of nanosized layered structures. At the nanometer scale, the understanding of the dielectric response demands a proper treatment of the electronic structure and can no longer be inferred from macroscopic electrostatics. Typical systems exhibiting such effects include quantum-confined structures and thin films.

Quantum confined silicon structures, such as quantum dots^{1,2} and quantum wells,³ have been the object of recent investigations. It is generally recognized that these structures exhibit a lower dielectric permittivity than bulk Si. However, it has been questioned only recently whether this behavior results from surface rather than from bulk effects.³

Thin-film metrology on dielectric layers critically relies on the availability of models for the spatial variation of the dielectric response.^{4,5} This issue has currently acquired importance in the context of silicon technology. Current research is focusing on the replacement of the gate oxide SiO₂ by a material of higher dielectric permittivity.⁶ The formation of an undesired silica layer at the interface between silicon and the alternative dielectric affects the overall permittivity of the gate-oxide stack and carries direct implications for the scalability of future microelectronics devices.

Both examples illustrated above call for the determination of an atomic-scale dielectric permittivity profile across lay-

ered structures. In principle, the dielectric response is completely accounted for by the nonlocal dielectric tensor $\chi_{ij}(\mathbf{r}, \mathbf{r}'; \omega)$.⁷ However, the calculation of this quantity for complex systems is computationally demanding,⁸ and often carries excessively detailed information with respect to experimental interests.

In a recent paper, we introduced a theoretical scheme for investigating polarization profiles across interfaces between adjacent dielectrics.⁹ The present work further develops this theory to access the corresponding permittivity profiles. In addition, we are able to identify localized contributions to the permittivity profile through the use of maximally localized Wannier functions, thereby highlighting the role of specific atomic-scale structural features.

The present approach is illustrated through applications to silicon slabs and Si-SiO₂ interfaces. From the local permittivity profile across silicon slabs of finite thickness, we investigate the origin of the size-dependent permittivity. Our analysis indicates that the variation of the permittivity relates to the reduced screening of the outermost Si planes. This effect becomes progressively more important as the surface-to-volume ratio increases, and explains the reduction of the average slab permittivity with decreasing thickness. In our investigation of the Si(100)-SiO₂ interface, we determine the local permittivity profile across the interface for two different Si(100)-SiO₂ model structures. We show that bulk permittivities are recovered within distances from the interface corresponding to a few bond lengths and that the local permit-

tivity is enhanced in the interfacial suboxide region. In particular, we introduce Si-centered polarizable units and show that the corresponding polarizabilities vary with the oxidation state of the central Si atom. We therefore associate the dielectric transition at the Si-SiO₂ interface to the chemical grading.

The present paper is organized as follows. Section II outlines our theory for obtaining a local permittivity profile. In particular, we show how the electronic permittivity profile can be decomposed in discrete contributions pertaining to maximally localized Wannier functions. Similarly, we decompose the lattice contribution to the permittivity into discrete ionic polarizabilities. In Sec. III, we specify the technical details of our specific computational approach. Sections IV and V are devoted to applications to Si slabs and Si-SiO₂ interfaces, respectively. The conclusions are drawn in Sec. VI.

II. THEORY OF LOCAL PERMITTIVITY

A. Permittivity profile

We introduce a procedure for calculating the dielectric permittivity profile of an insulating material along a given direction. Our approach is based on the definition of a *microscopic* polarization through the transient current induced by an electric field.¹⁰ This approach carries the advantage that the polarization field is well defined down to atomistic length scales and does not suffer from any gauge arbitrariness.¹¹

In the linear regime and in stationary conditions, an applied microscopic electric field $e_i(\mathbf{r}; \omega)$ induces a microscopic polarization $p_i(\mathbf{r}; \omega)$ given by

$$p_i(\mathbf{r}; \omega) = \int d\mathbf{r}' \chi_{ij}(\mathbf{r}, \mathbf{r}'; \omega) e_j(\mathbf{r}'; \omega), \quad (1)$$

where $\chi_{ij}(\mathbf{r}, \mathbf{r}'; \omega)$ denotes the microscopic dielectric susceptibility tensor, ω corresponds to the frequency of the applied field, and the indexes indicate Cartesian directions. In Eq. (1), the electric field $e_i(\mathbf{r}; \omega)$ includes the self-consistent response of the system to the external applied field. The frequency ω appearing in Eq. (1) is here assumed to be smaller than typical electronic excitation energies.

In this work, we are interested in defining a dielectric permittivity which varies in the x direction on length scales corresponding to interatomic distances. For this purpose, we smooth atomic scale fluctuations of the charge density in the x direction by a convolution with a Gaussian kernel. The width of this kernel then defines the typical length scale over which variations of the permittivity are meaningful. In the orthogonal directions, we consider macroscopic planar averages. Under these conditions, the dielectric susceptibility takes the form

$$\chi_{ij}(\mathbf{r}, \mathbf{r}'; \omega) \approx \chi_i(x; \omega) \delta(\mathbf{r} - \mathbf{r}') \delta_{ij}, \quad (2)$$

where the off-diagonal components vanish because of the planar average.

In Eq. (2), we assume in addition that the dielectric response is local. This assumption of locality is well justified

when averages over interatomic distances are considered. Indeed, for insulators, the homogeneous real-space dielectric function generally decays with a characteristic length of the order of interatomic distances. For instance, we estimated decay lengths of 0.7 Å for SiO₂ and of 1.7 Å for Si (see Appendix A).

Combining Eqs. (1) and (2), we obtain

$$\bar{\bar{p}}_x(x; \omega) = \chi(x; \omega) \bar{\bar{e}}_x(x; \omega), \quad (3)$$

where the double bars indicate the average over the yz plane and the Gaussian filter. In Eq. (3), we dropped the Cartesian index of the dielectric susceptibility specifying the x direction. In the following, we will refer to $\chi(x; \omega)$ as to the *local* susceptibility and

$$\varepsilon(x; \omega) \equiv 1 + 4\pi\chi(x; \omega) \quad (4)$$

as the corresponding *local* permittivity.

In Eq. (3), the electric field $\bar{\bar{e}}_x(x; \omega)$ is obtained from the induced charge density ρ_{ind} through the Gauss relation

$$\frac{d}{dx} \bar{\bar{e}}_x(x; \omega) = 4\pi \bar{\bar{\rho}}_{\text{ind}}(x; \omega). \quad (5)$$

The induced polarization $\bar{\bar{p}}_x(x; \omega)$ is defined through the transient current induced by an electric field.¹⁰ However, in the case of one-dimensional systems, this polarization can be obtained following an alternative procedure. In general, the equation

$$\nabla \cdot \mathbf{p}(\mathbf{r}; \omega) = -\rho_{\text{ind}}(\mathbf{r}; \omega) \quad (6)$$

specifies the polarization within a divergence-free vector field. For one-dimensional systems, the planar average of the latter field vanishes and the polarization $\bar{\bar{p}}_x$ satisfies the relation

$$\frac{d}{dx} \bar{\bar{p}}_x(x; \omega) = -\bar{\bar{\rho}}_{\text{ind}}(x; \omega). \quad (7)$$

Equations (5) and (7) give the electric field $\bar{\bar{e}}_x$ and the polarization $\bar{\bar{p}}_x$, respectively, up to two additive constants. For a finite system, the first constant is fixed by the requirement that the electric field away from the system equals the external field, while the second constant is fixed by the condition that the induced polarization vanishes in the region with vanishing charge density. At variance, when an extended periodic model is adopted, the unknown constant in $\bar{\bar{e}}_x$ is determined by the average selfconsistent electric field in the supercell, while the corresponding term in $\bar{\bar{p}}_x$ is determined by the macroscopic Berry-phase polarization.

When the calculation is performed within a supercell, it is convenient to express the local susceptibility in terms of the polarization $\bar{\bar{p}}_x$. From Eqs. (3), (5), and (7), we obtain

$$\frac{4\pi\chi(x; \omega)}{1 + 4\pi\chi(x; \omega)} = \left(1 - \frac{1}{\varepsilon(\omega)}\right) \frac{\bar{\bar{p}}_x(x; \omega)}{\langle \bar{\bar{p}}_x(x; \omega) \rangle}, \quad (8)$$

where $\langle \cdots \rangle$ indicate an average over the simulation cell and $\varepsilon(\omega)$ corresponds to the permittivity of the full cell

$$\varepsilon(\omega) \equiv 1 + 4\pi \frac{\langle \bar{p}_x(x; \omega) \rangle}{\langle \bar{e}_x(x; \omega) \rangle}. \quad (9)$$

We note that Eqs. (4), (7), and (8) establish a direct link between the induced charge density and the local permittivity regardless of the frequency ω . Thus, the derived relations hold in particular for the electronic $\varepsilon^\infty(x)$ and the static $\varepsilon^0(x)$ permittivities.

In practical applications, it is often convenient to define a permittivity pertaining to a slab of finite thickness, delimited by the planes $x=x_1$ and $x=x_2$. From Eqs. (3)–(5) and (7), one derives

$$\frac{\partial}{\partial x} [\varepsilon(x, \omega) \bar{e}_x(x, \omega)] = 0, \quad (10)$$

which is analogous to the conservation of the component of the displacement field orthogonal to the interfaces in classical electrostatics. This analogy is also at the basis of the following relation which holds between the permittivity of the slab $\varepsilon([x_1, x_2]; \omega)$ and the local permittivity $\varepsilon_x(x, \omega)$:

$$\varepsilon([x_1, x_2]; \omega) = \frac{1}{x_2 - x_1} \int_{x_1}^{x_2} \frac{1}{\varepsilon(x, \omega)} dx. \quad (11)$$

B. Wannier decomposition of the permittivity profile

To analyze the dielectric properties at the atomic scale, we describe the electronic structure in terms of localized Wannier functions.¹² A given decomposition in Wannier functions directly defines a partition of the electronic charge density in localized contributions. We here restrict the discussion to a single-particle description. While we refer to the Wannier terminology pertaining to extended periodic systems, the same concepts apply in a fully equivalent way to finite systems.

For an insulator in an electric field \mathcal{E} , the material state of interest corresponds to a long-living excited state,¹⁴ for which the density matrix preserves the periodicity of the ground state and its insulatorlike properties.^{15,16} Hence, for this state, it remains possible to define a set of localized Wannier functions $\{w_n^{\mathcal{E}}\}$. By continuity, an unambiguous one-to-one correspondence can be established between these polarized Wannier functions and the respective ones in absence of electric field $\{w_n^{\mathcal{E}=0}\}$. This correspondence defines a partition of the induced charge density in localized contributions $\rho_{\text{ind}}^{(n)} = |w_n^{\mathcal{E}}|^2 - |w_n^{\mathcal{E}=0}|^2$:

$$\bar{\rho}_{\text{ind}} = \sum_n \bar{\rho}_{\text{ind}}^{(n)}, \quad (12)$$

where the double bars correspond to the double averages defined in Sec. II A. The localized contributions to the dipole density $\bar{p}_x^{(n)}(x; \omega)$ are then defined through the analogous of Eq. (7):

$$\frac{d}{dx} \bar{p}_x^{(n)}(x; \omega) = -\bar{\rho}_{\text{ind}}^{(n)}(x; \omega). \quad (13)$$

When integrating Eq. (13), we fix the unknown constant through the condition

$$A \int_{-\infty}^{\infty} \bar{p}_x^{(n)}(x; \omega) dx \equiv e(x_n^{\mathcal{E}} - x_n^{\mathcal{E}=0}), \quad (14)$$

where A corresponds to the transverse area of the simulation cell, e is the electron charge, and $x_n^{\mathcal{E}}$ stands for the center of the Wannier function $w_n^{\mathcal{E}}$. This choice ensures that the sum of the individual contributions gives the full induced polarization

$$\begin{aligned} A \int_0^{L_x} \bar{p}_x(x; \omega) dx &\equiv A \int_0^{L_x} \sum_n \bar{p}_x^{(n)}(x; \omega) dx = \sum_n e(x_n^{\mathcal{E}} - x_n^{\mathcal{E}=0}) \\ &= \Omega(P_x^{\mathcal{E}} - P_x^{\mathcal{E}=0}), \end{aligned} \quad (15)$$

where Ω is the volume of the simulation cell. In Eq. (15), the integral extends over a periodic cell and the sum over the corresponding Wannier functions. The assignment in Eq. (14) is therefore consistent with the way we determined the constant when integrating Eq. (7). The last equality in Eq. (15) results from the very basic definition of the Berry-phase polarization (denoted by P_x).¹⁷

To evaluate the contribution to the local susceptibility $\chi^{(n)}(x; \omega)$ resulting from each Wannier function, we proceed along the same lines as in Sec. II A:

$$\bar{p}_x^{(n)}(x; \omega) = \chi^{(n)}(x; \omega) \bar{e}_x(x; \omega). \quad (16)$$

Repeating the derivation which led to Eq. (8), we obtain

$$\frac{4\pi\chi^{(n)}(x; \omega)}{1 + 4\pi\chi(x; \omega)} = \left(1 - \frac{1}{\varepsilon(\omega)}\right) \frac{\bar{p}_x^{(n)}(x; \omega)}{\langle \bar{p}_x(x; \omega) \rangle}, \quad (17)$$

which relates the dipole density associated to a Wannier function to the corresponding local susceptibility. From Eq. (17), it follows immediately that

$$\varepsilon(x; \omega) = 1 + \sum_n 4\pi\chi^{(n)}(x; \omega). \quad (18)$$

For one-dimensional systems, it is convenient to use Wannier functions *maximally* localized in the x direction, the so-called hermaphrodite Wannier functions.¹³ Since the typical localization length of such functions is of the order of bond lengths,¹³ the resulting decomposition of the local susceptibility $\chi(x; \omega)$ turns out to be particularly suitable for assigning variations of the local susceptibility to specific structural features, as we demonstrate in the following sections. Furthermore, hermaphrodite Wannier functions carry a special significance, since they are eigenstates of the one-dimensional position operator in extended systems.¹³

C. Decomposition in discrete polarizabilities

An alternative way to investigate the variation of the local permittivity consists in decomposing the continuous dielectric medium in discrete units. In this section, we consider separately the electronic and ionic responses to the electric field.

1. Electronic polarizabilities

Using the decomposition introduced in Sec. II B, we define an *effective* electronic polarizability $\alpha_{\text{elec}}^{(n)}$ for each Wan-

nier function by relating its induced dipole to the electric field at its center x_n :

$$e(x_n^\varepsilon - x_n^{\varepsilon=0}) \equiv \alpha_{\text{elec}}^{(n)} \bar{e}_x(x_n), \quad (19)$$

where the same approximations leading to Eq. (3) are assumed. To make connection with Sec. II B, we point out that there is a simple relationship between the effective polarizabilities $\alpha_{\text{elec}}^{(n)}$ and the contribution to the local susceptibility of a given Wannier function $\chi^{(n)}(x)$. Using Eqs. (14) and (16), one derives

$$\alpha_{\text{elec}}^{(n)} = \frac{A}{\bar{e}_x(x_n)} \int_0^{L_x} \chi^{(n)}(x) \bar{e}_x(x) dx. \quad (20)$$

Using the last equality in Eq. (15), we then recover the electronic permittivity of the full simulation cell as follows:

$$\varepsilon_\infty = 1 + \frac{4\pi}{\Omega} \sum_n \frac{\bar{e}_x(x_n)}{\langle \bar{e}_x(x) \rangle} \alpha_{\text{elec}}^{(n)}. \quad (21)$$

In particular, when the effective field is slowly varying, as for instance well inside homogeneous regions, Eq. (20) simplifies to

$$\alpha_{\text{elec}}^{(n)} = A \int_0^{L_x} \chi^{(n)}(x) dx, \quad (22)$$

establishing a transparent relation with the local susceptibility of the Wannier function $\chi^{(n)}(x)$. Similarly, Eq. (21) reduces to

$$\varepsilon_\infty = 1 + \frac{4\pi}{\Omega} \sum_n \alpha_{\text{elec}}^{(n)}. \quad (23)$$

2. Ionic polarizabilities

With the same spirit as for the electronic polarizabilities, we define effective ionic polarizabilities through the induced dipole associated to a given ion. The latter can be expressed in terms of the induced ionic displacement and the corresponding dynamical charge.

In nonhomogeneous systems such as superlattices, the local electric field might present significant spatial variations. In order to define truly local quantities, we introduce in this work dynamical charges ζ_I which are defined with respect to the effective local field \bar{e}_x rather than to the macroscopic field

$$\zeta_{I,x\alpha} \equiv \frac{\partial F_{I,\alpha}}{\partial \bar{e}_x(R_{I\alpha})}, \quad (24)$$

where $F_{I\alpha}$ and $R_{I\alpha}$ indicate the ionic force and coordinate along the x axis, respectively. The dynamical charges ζ_I are related to the Born (Z_I^B) and Callen (Z_I^C) charges¹⁸ through

$$\zeta_{I,x\alpha} = \frac{\varepsilon^\infty(x)}{\varepsilon^\infty} Z_{I,x\alpha}^B = \varepsilon^\infty(x) Z_{I,x\alpha}^C, \quad (25)$$

where $\varepsilon^\infty(x)$ corresponds to the local electronic permittivity introduced in Sec. V B and ε^∞ is the electronic permittivity of the simulation cell. In the homogeneous regions on both sides of a heterojunction, the charges ζ_I defined by Eq. (24)

reduce to the Born charges of the corresponding bulk materials.

In analogy with the electronic polarizabilities in Eq. (19), we then define an effective ionic polarizability as

$$\sum_\alpha \zeta_{I,x\alpha} (R_{I\alpha}^\varepsilon - R_{I\alpha}^{\varepsilon=0}) \equiv \alpha_{\text{ion}}^{(I)} \bar{e}_x(R_{I\alpha}). \quad (26)$$

From the ionic contribution to the induced macroscopic polarization along x ,¹⁹

$$P_{x,\varepsilon}^{\text{ion}} - P_{x,\varepsilon=0}^{\text{ion}} = \frac{1}{\Omega} \sum_{I,\alpha} Z_{I,x\alpha}^B (R_{I\alpha}^\varepsilon - R_{I\alpha}^{\varepsilon=0}), \quad (27)$$

the lattice contribution to the static permittivity is obtained as

$$\varepsilon_0 - \varepsilon_\infty = 4\pi \frac{P_{x,\varepsilon}^{\text{ion}} - P_{x,\varepsilon=0}^{\text{ion}}}{\langle \bar{e}_x(x) \rangle}. \quad (28)$$

From Eqs. (25)–(28), we then derive the explicit relation between the effective ionic polarizabilities and the permittivity of the full simulation cell:

$$\varepsilon_0 - \varepsilon_\infty = \frac{4\pi}{\Omega} \sum_I \frac{\varepsilon^\infty}{\varepsilon^\infty(R_{I\alpha})} \frac{\bar{e}_x(R_{I\alpha})}{\langle \bar{e}_x(x) \rangle} \alpha_{\text{ion}}^{(I)}. \quad (29)$$

When the effective field and the electronic permittivity vary slowly, as for instance inside homogeneous regions, Eq. (29) simplifies to

$$\varepsilon_0 - \varepsilon_\infty = \frac{4\pi}{\Omega} \sum_I \alpha_{\text{ion}}^{(I)}. \quad (30)$$

III. PRACTICAL IMPLEMENTATION

A. General methods

The calculations described in this work were performed adopting a generalized gradient approximation to density functional theory.²⁰ We accounted for valence electronic states using a pseudopotential scheme.²¹ We adopted a norm-conserving pseudopotential for Si atoms²² and ultrasoft ones for O and H atoms.²³ The wave functions and the charge density were expanded in plane-wave basis sets with kinetic energy cutoffs of 24 and 150 Ry, respectively. The Brillouin zone of the investigated systems were sampled at the Γ point. Structural relaxations were performed within a damped molecular dynamics approach,²⁴ and carried on until the ionic forces were smaller than 0.005 eV/Å.

In this work, we are mainly concerned with extended periodic systems. We calculated the static and high-frequency dielectric permittivities through the application of a finite electric field, as described in Ref. 25 within the context of the Berry-phase theory of the polarization,^{17,26} unless specified otherwise. The induced charge density appearing in Eqs. (5)–(7) was evaluated by calculating the difference between the charge densities corresponding to two opposite macroscopic electric fields. The local dielectric permittivity was then derived as described in Sec. II A. We note that, in the case of finite systems (see Sec. IV B), the local dielectric response can also be obtained through the application of a simple saw-tooth potential.

The smoothing required to remove nonlocality effects was performed by means of a Gaussian kernel with a standard deviation of 1 Å. With this kernel, the smoothed polarization and electric fields vary by less than 1% well inside the bulk components (see Appendix C).

To obtain Wannier functions maximally localized along the x direction, we made use of the algorithm described in Ref. 27. This procedure consists in determining the unitary transformation which minimizes the off-diagonal matrix elements of the position operator.²⁸ We note that, at the Γ point, the position operator is non-Hermitian.¹³ Therefore, the optimal unitary transformation does not diagonalize this operator exactly,¹³ and the centers $\{x_n\}$ of the resulting Wannier functions

$$x_n \equiv \frac{L_x}{2\pi} \Im \ln \langle w_n | e^{i2\pi x/L_x} | w_n \rangle, \quad (31)$$

only approximately correspond to the eigenvalues of the position operator. This difference affects the last equality in Eq. (15). However, this effect vanishes in the limit of large supercell size.¹³ Indeed, we found that such differences amount to at most 1% for the large supercells in our calculations.

B. Bulk permittivities: convergence issues

In this work, we determine the permittivity using a finite-field approach with a Γ -point sampling. The permittivity is obtained by taking finite differences of the polarization with respect to the electric field.²⁵ Two issues deserve attention and are addressed in the present section.

First, it is important to determine the range of electric fields in which the polarization scales linearly. In view of the systems considered in this work, we here focus on bulk Si. We calculated the susceptibility of a bulk Si sample as a function of the electric field \mathcal{E}_x . We considered a simulation cell of size $L_x = 21.94$ Å in the $[100]$ direction (16 MLs), with a transverse 2×2 repeat unit. Figure 1 shows that the dielectric response is almost linear up to a field of 0.001 a.u. Beyond this value, the permittivity progressively increases until the electric field value of 0.01 a.u., beyond which the electronic structure could no longer be converged.²⁵ Since the numerical convergence is faster for larger fields, we chose to work with an optimal value for the electric field given by $\mathcal{E}_x L_x = 0.001 \times 21.94$ a.u. Å.

The second issue corresponds to the scaling of the permittivity with the simulation cell size L_x . This issue relates to the choice of sampling the Brillouin zone of the simulation cell with the sole Γ point, and therefore corresponds to the study of the k -point convergence.²⁹ For this purpose, we calculated the permittivity of bulk Si using simulation cells with the same transverse size as above but with varying L_x (Fig. 1). For large cell parameters ($L_x > 20$ Å), we found a L_x^{-2} behavior,²⁹ and we extrapolated the trend to obtain a converged value of $\epsilon_{\text{Si}} = 14.3$. Given the limited yz sampling of the Brillouin zone in the present calculation, this converged value differs from that determined with a full k -point sampling, overestimating the latter value by 13%.³⁰

The bulk permittivity of Si calculated here constitutes a reference value for the subsequent analysis of the local per-

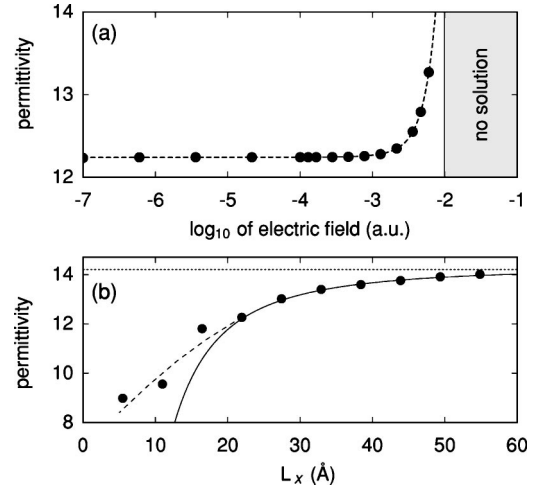


FIG. 1. (a) Permittivity of bulk Si as a function of the electric field (disks). The region where the electronic structure could not be converged is shaded. (b) Permittivity of bulk Si as a function of the size of the simulation cell L_x (disks). The solid line corresponds to the L_x^{-2} limiting behavior. The dotted line indicates the value extrapolated for an extended system. Dashed lines in (a) and (b) are guides to the eye.

mittivity. Similarly, we determined such a reference for bulk SiO_2 . For this purpose, we considered a β -cristobalite model of SiO_2 with lattice parameters adapted to match the Si lattice (see Sec. V A). We used the same electric field as for silicon, since the larger band gap of SiO_2 ensures that this field falls within the linear regime. The dependence of the electronic and static permittivities with cell size shows a L_x^{-2} asymptotic behavior. Extrapolation to infinite cell size gives an electronic permittivity of $\epsilon_{\text{SiO}_2}^\infty = 2.0$ and a static permittivity of $\epsilon_{\text{SiO}_2}^0 = 3.8$.

At this stage, it is worth noting that the convergence with k -point sampling of the local permittivity of a layered system is more demanding than the convergence of the corresponding overall permittivity. Indeed, while the induced charge density appearing in Eq. (7) rapidly converges with the Brillouin zone sampling, the Berry-phase polarization which enters \bar{p}_x through the additive constant does not. As a result, when the macroscopic polarization is converged within an error δ , the corresponding error on the local permittivity is $\sim \epsilon(x)\delta$. In the case of the Si- SiO_2 interface considered in this work, this effect counteracts the overestimation due to the transverse Brillouin zone sampling and brings the permittivity of the Si region close to the fully converged value (see Secs. IV A and V B).

IV. LOCAL PERMITTIVITY IN SILICON SLABS

A. Bulk Si with a defect layer

To illustrate our procedure for determining the local dielectric permittivity (Sec. II), we focus in this section on a model system with a localized defect layer. We first considered a bulk Si system with a supercell containing 16 ML in the $[100]$ direction and a 2×2 repeat unit in the orthogonal plane. Using a finite electric field,²⁵ we calculated a permit-

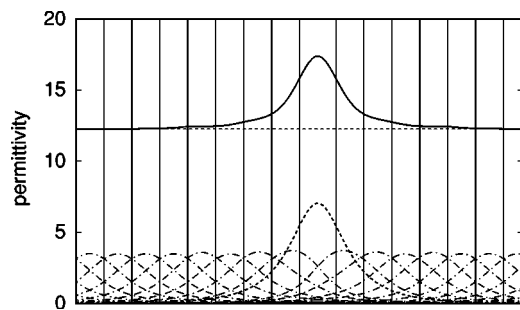


FIG. 2. Local permittivity profile (solid) along the [100] direction in bulk Si, presenting a defective layer with a larger interplanar separation. The horizontal dashed line corresponds to the permittivity of the regular structure. Contributions to the local permittivity resulting from maximally localized Wannier functions of the defective (dotted) and regular (dash-dotted) Si layers are also shown. Vertical lines represent planes of Si atoms.

tivity of 12.3 for this system. Next, we introduced the following perturbation: we increased the supercell size L_x in the [100] direction while maintaining all the (100) interplane separations but one at the equilibrium distance. In the resulting structure, all Si-Si bond distances are at equilibrium (2.37 Å) except those corresponding to the larger interplane separation (2.63 Å). Furthermore, the latter bonds are slightly tilted towards the [100] direction. In Fig. 2, we show the local susceptibility profile as a function of a coordinate along the [100] direction. An enhancement of the local susceptibility is observed in correspondence of the stretched layer. At a distance of about two monolayers from the defect, the bulk Si value is essentially recovered. To understand this behavior, we decomposed the local susceptibility in localized contributions pertaining to maximally localized Wannier functions of individual layers (Fig. 2). It is evident that all the regular Si-Si bonds give very similar contributions, irrespective of their location with respect to the defective bonds. In particular, these regular contributions are fully consistent with the susceptibility of the undefected system. On the other hand, the defective layer shows a much larger susceptibility, which is responsible for the observed enhancement of the local screening. This example demonstrates the effectiveness of our approach both in mapping the local dielectric permittivity and in assigning its variations to specific structural features.

B. Silicon slabs

In this section, we study the effect of the finite size on the high-frequency dielectric permittivity of Si quantum wells by performing a local analysis as outlined in Sec. II A. The quantum confinement of the electrons in a system of finite size induces a blueshift of the optical absorption spectrum.^{31,32} Since the absorption spectrum is directly related to the real part of the dielectric function through the Kramers-Krönig relations, it has been suggested that the confinement should affect the dielectric permittivity.³³ The decrease of the electronic permittivity with size has already been predicted for various silicon nanostructures.^{1,2} However, methods based on macroscopic approaches are not able

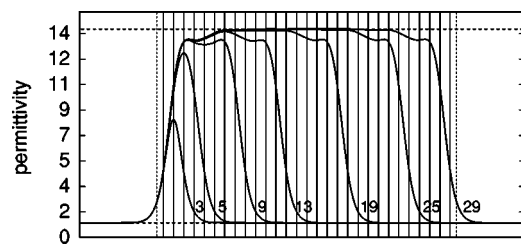


FIG. 3. Permittivity profiles along the [100] direction for Si(100) slabs with H-terminated surfaces. The numbering refers to the slab size in terms of Si planes. Vertical lines represent planes of Si (solid) and H (dotted) atoms for the largest considered slab. All the slabs are aligned through the positions of the H atoms of the surface on the left. The permittivities of the extended bulk (14.3) and of the vacuum are indicated by horizontal lines.

to establish whether the size dependence of the permittivity arises from a quantum confinement effect, or from the increased surface-to-volume ratio in small nanostructures.^{1,2} Recent work supports that quantum confinement has a negligible effect, the permittivity reduction being essentially due to the lower polarizability at the surfaces.³

Here, we considered Si slabs with (100) surfaces. We used a periodic repeat unit of 2×2 in the planes parallel to the surfaces. The slabs were terminated by H atoms, with Si-H bond lengths as in silane (1.5 Å) and H-Si-H angles at the tetrahedral value. To investigate the size dependence of the slab permittivity, we calculated the local permittivity profiles for Si slabs with thicknesses ranging between 0.5 and 4 nm, corresponding to 3 and 29 MLs, respectively. We included a finite electric field in our calculation through a sawtooth-shaped potential, and we fixed the unknown constant in Eq. (7) by requiring that the microscopic polarization vanishes in the middle of the vacuum region of the simulation cell. This approach allowed us to avoid the convergence issues related to the Berry-phase polarization. Figure 3 shows that, beyond a critical size of 13 MLs, the permittivity profile in the slab interior is flat and closely matches (within 1%) the bulk value of $\epsilon_B = 14.3$ determined in Sec. III B, while the local permittivity in the outermost Si planes decreases as the surface is approached. For slabs with less than 13 MLs, the permittivity of the inner layers is appreciably smaller than the bulk Si value, and decreases with decreasing thickness. Within this range, a detailed analysis of the Wannier function contributions to the local permittivity reveals that the Si-H bonds at the surface and the Si-Si bonds between the two outermost Si planes exhibit a reduced polarizability if compared to bulk Si-Si bonds. As a result, when the slab is thinner than 13 MLs, the proximity of the surfaces prevents the inner layers from reaching the bulk value. Overall, the combined effect of an inner region with the permittivity of bulk Si and of two outer regions with lower permittivities results into an average value which approaches the bulk permittivity rather slowly with increasing thickness. This is shown in Fig. 4(a), where we compare the local permittivity in the central Si plane with the average permittivity over the slab. To evaluate the average permittivity, we used Eq. (11) with the slab boundaries taken at the outermost Si planes. This choice sets the slab thickness d equal to the distance between the farthest Si layers.

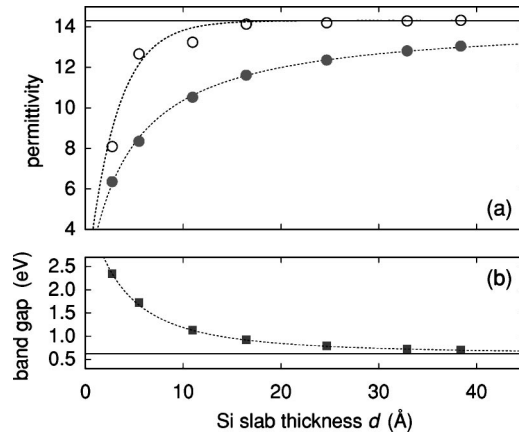


FIG. 4. (a) Permittivity of a Si slab as a function of thickness d : local permittivity in the central Si plane (circles) compared to the overall slab permittivity (disks). The horizontal line indicates the permittivity of a slab of infinite thickness (14.3), as determined in Sec. III B. The dashed lines are guides to the eye. (b) Band gap of a Si slab as a function of thickness d (squares). The horizontal line indicates the band gap of a slab of infinite thickness (0.62 eV). The dashed line is a guide to the eye.

In Fig. 4(b) we report for comparison the band gaps of the considered Si slabs. The dependence of the Si band gap on slab thickness approximately follows the d^{-2} behavior expected for an infinite potential well, and agrees with previous calculations within 0.1 eV.³⁴ While the relative band gap reduction from the slab with 13 Si MLs to the one with 31 MLs is $\sim 30\%$, the corresponding increase in the permittivity of the inner layers is $\sim 1\%$, indicating that the band gap and the permittivity are not correlated. This finding can be rationalized by considering that the permittivity depends on the whole absorption spectrum and not only on the band gap energy.

To summarize our results on hydrogen-terminated Si(100) slabs, quantum confinement is found to have a negligible effect on the permittivity, at least beyond a critical thickness corresponding to 13 Si MLs. Furthermore, the reduction of the average slab permittivity with decreasing thickness originates from the increasing surface-to-volume ratio. Despite the rather different methodological approaches, our results are in good overall agreement with the calculations of Ref. 3.

V. LOCAL PERMITTIVITY AT THE Si-SiO₂ INTERFACE

A. Interface models

To construct model Si(100)-SiO₂ interfaces, we matched pseudomorphically ideal β -cristobalite to Si(100). The Si lattice parameter was chosen equal to 5.48 Å, corresponding to the relaxed lattice constant in our theoretical framework. The lattice parameter of the oxide in the [100] direction was determined by a separate relaxation, which gave a Si-O bond length of 1.63 Å, Si-O-Si angles of 179°, and O-Si-O angles of 114.6° and 107.0°. The density of the relaxed structure is 1.9 g/cm³, about 15% lower than the experimental value (2.2 g/cm³).

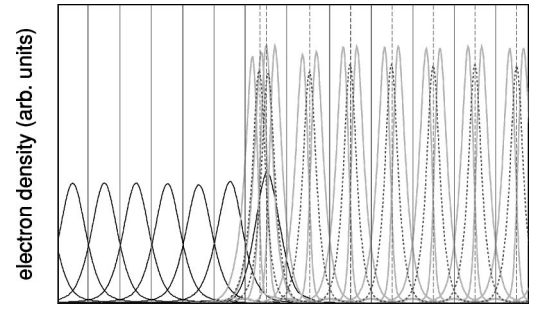


FIG. 5. Planar average of the Wannier-function charge densities corresponding to model I of the Si-SiO₂ interface: Si-Si bonds (black solid), Si-O bonds (gray solid), and nonbonding O orbitals (black dotted). The horizontal axis is oriented along the [100] direction. Vertical lines represent planes of Si (solid) and O (dotted) atoms.

In order to obtain a structural transition without coordination defects between the substrate and the oxide in our model interfaces, we adopted two different interface constructions, models I and II, which correspond to those reported in Refs. 35 and 36, respectively. In model I, the transition region extends over about 3 Å and includes 1 monolayer (ML) of Si⁺¹ and 0.5 ML of Si⁺² partially oxidized Si atoms, with an average stoichiometry of SiO_{0.7}. In model II, all the partial oxidation states of Si, Si⁺¹, Si⁺², and Si⁺³, appear in equal amounts of 0.5 ML each. The thickness of the suboxide region is about 3 Å, and its average stoichiometry is SiO_{1.0}. Overall, the amount and the spatial distribution of the suboxides in both models qualitatively agree with photoemission measurements.^{37,38}

For each interface model, we constructed corresponding Si-SiO₂-Si superlattices by mirroring the interface structures. These superlattices contain 13 Si layers (≈ 16 Å) and 10 SiO₂ molecular layers (≈ 18 Å). In the plane of the interface, we used a 2×2 interface Si unit. We determined an optimal supercell size in the direction orthogonal to the interface planes, by separately relaxing a corresponding interface structure with exposed surfaces saturated by H atoms. The choice of β -cristobalite as a model oxide allowed us to build Si-SiO₂-Si superlattices with equivalent Si-SiO₂ and SiO₂-Si interfaces. In this way, dipolar effects arising from asymmetric interface structures were avoided.

The relaxed structures of both superlattices showed typical bond lengths and bond angles.^{35,39,40} We found an average Si-O bond length of 1.63 Å in the stoichiometric oxide. In the suboxide region, we found slightly larger bond distances (1.67–1.74 Å), consistently with the less electronegative environment.^{39,40} The Si-O-Si and O-Si-O bond angles in the SiO₂ layers remain close to those of the corresponding bulk oxide.

The electronic structure of the model Si-SiO₂-Si superlattices is conveniently described in terms of Wannier functions maximally localized along the direction orthogonal to the interfaces (Sec. III A). In Fig. 5, we show the yz average of the charge density associated to these functions for model I of the Si-SiO₂ interface. Outside of the suboxide region, both on the Si and SiO₂ side of the interface, the shape of the Wannier functions is almost independent of position. The

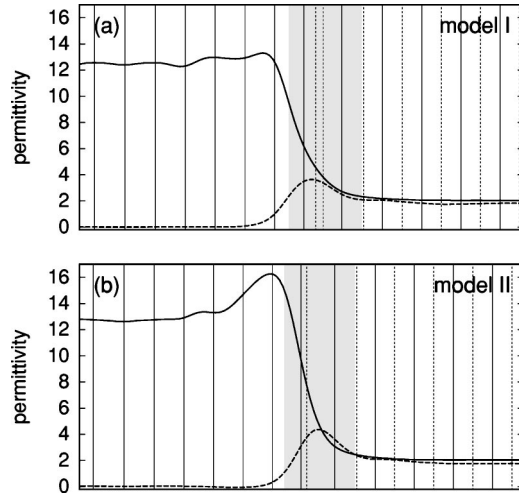


FIG. 6. Permittivity profiles across (a) model I and (b) model II of the Si-SiO₂ interface: electronic permittivity (solid) and lattice contribution $\epsilon_0(x) - \epsilon_\infty(x)$ (dashed). Vertical lines indicate planes of Si (solid) and O (dotted) atoms. The shaded area represents the suboxide transition layer.

Wannier functions can be partitioned into three classes according to the location of their centers and the magnitude of their spreads.²⁸ At the Si-SiO₂ interface, we distinguish Wannier functions associated to Si-Si bonds, Si-O bonds, and nonbonding O orbitals. For the Wannier spreads of Si-Si bonds, Si-O bonds, and nonbonding O orbitals, we found 0.83 ± 0.05 , 0.43 ± 0.01 , and 0.40 ± 0.01 Å, respectively. Hence the spread of the Wannier functions is a typical signature of the nature of these localized electronic states.

B. Permittivity profile across the interface

Following the procedure outlined in Sec. II A, we calculated the *local* permittivity profiles along a direction normal to the interfaces for models I and II (Fig. 6). These profiles can be obtained separately for the electronic and ionic permittivities.

The local electronic permittivity varies across the interface, decreasing from the silicon value to the SiO₂ one. The transition is about 6 Å thick and includes the full suboxide region. In the stoichiometric oxide, the electronic permittivity is constant and starts increasing only within the suboxide region. This result is consistent with recent Auger measurements which showed that the oxide permittivity agrees with that of bulk SiO₂ for distances from the interface larger than 6 Å.⁴¹ To understand the enhancement of the local electronic permittivity on the silicon side of the interface, we carried out the decomposition into Wannier contributions introduced in Sec. II B (Fig. 7). This decomposition shows that the observed bumps result from asymmetric dipolar contributions associated to Si-Si bonds of the suboxide, peaked towards the interior of the silicon slab (see Appendix B). This contribution is larger in model II, since (i) the number of Si-Si bonds in this model is about 30% larger than in model I and (ii) the Si-Si bonds in model II are more polarizable than in model I due to their larger average bond length (2.66 Å in

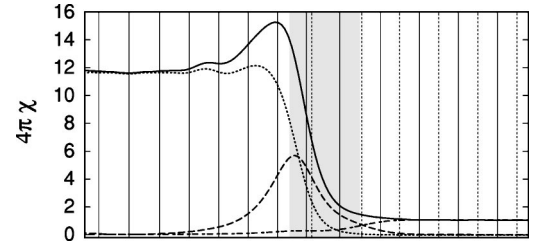


FIG. 7. Profile of the local electronic susceptibility across model II of the Si(100)-SiO₂ interface (solid line). Contributions to the susceptibility arising from Wannier functions of the Si slab (dotted), the suboxide (dotted), and the oxide (dash-dotted) are shown separately. The shaded area represents the suboxide transition layer. Vertical lines indicate planes of Si (solid) and O (dotted) atoms.

model II vs 2.52 Å in model I). The latter effect is consistent with the discussion in Sec. IV A. We refer to Appendix B for a detailed analysis of the origin of this effect.

We obtained the ionic contribution to the permittivity given in Fig. 6 by replacing the ionic point charges by Gaussian functions with standard deviations of 1 Å. In the stoichiometric oxide, the ionic contribution assumes a constant value corresponding to bulk SiO₂ (see Sec. III B). Similarly, the ionic contribution vanishes in the silicon bulk, because of the vanishing dynamical charges (see Sec. V C). In the suboxide, the ionic contribution is found to exceed the SiO₂ bulk value in both models. Since the dynamical charges are found to show a nearly linear dependence on the Si oxidation state (see Sec. V C), the origin of this enhancement should be assigned to the important structural relaxation of the suboxide atoms in response to an electric field.

For practical applications, it is convenient to approximate the permittivity profile through a three-layer model, assigning an average permittivity to each of the three regions Si, SiO_x, and SiO₂.^{9,42} We define the planes separating the silicon substrate and the suboxide on the basis of the amount of nonoxidized Si atoms and the bulk silicon density.⁹ We define similarly the separation between the suboxide and the stoichiometric oxide. Using Eq. (11), we obtain the individual slab permittivities given in Table I. Several comments are in order. First, the difference (1–2 %) between the static and electronic permittivities of the Si slabs results from the contribution of the outermost Si layers. Analogously, the permittivities of the SiO₂ layers are within 2% from those estimated for the bulk (Sec. III B), due to the slightly larger

TABLE I. Electronic (ϵ_∞) and static (ϵ_0) permittivities of the Si, SiO_x, and SiO₂ components of the Si(100)-SiO₂ model interfaces considered in this work. For each component, we also report separately the lattice contribution $\Delta\epsilon = \epsilon_0 - \epsilon_\infty$. Values between brackets correspond to the local permittivity in the middle of the Si slab.

	model I				model II			
	Si	SiO _x	SiO ₂		Si	SiO _x	SiO ₂	
ϵ_∞	12.6	(12.4)	3.8	2.1	13.5	(12.6)	5.0	2.1
ϵ_0	12.8	(12.4)	6.8	3.9	13.6	(12.6)	9.1	3.9
$\Delta\epsilon$	0.2	(0.0)	3.0	1.8	0.1	(0.0)	4.1	1.8

polarizability of the first oxide layer. Second, it is particularly satisfactory to note that the slab permittivities derived here from the local permittivity profile differ by less than 10% from the values derived in Refs. 9 and 42 and from a classical analysis. The small differences result from assigning *bulk* permittivities to the Si and SiO₂ slabs in the classical analysis. Thus the enhanced screening in the outermost Si and SiO₂ layers is effectively transferred to the suboxide. Third, note that the local permittivity in the Si interior (12.4 and 12.6 for models I and II, respectively) is smaller than the permittivity of an extended bulk, $\epsilon_{\text{Si}}=14.3$ (Sec. III B). This effect arises from the size dependence of the Berry-phase position operator in supercell calculations (Sec. III B).⁴³ Fourth, the suboxide shows a permittivity which is larger than that of bulk SiO₂: $\epsilon_{\text{SiO}_x}^0=6.8$ for model I and $\epsilon_{\text{SiO}_x}^0=9.1$ for model II (Table I), to be compared with $\epsilon_{\text{SiO}_2}^0=3.8$. This result is consistent with electrical measurements on Si-SiO₂-ZrO₂ gate stacks, which indicate that the oxide interlayer carries an enhanced permittivity ranging between 6 and 7.⁴⁴

C. Discrete electronic and ionic polarizabilities

In this section, we describe the local polarizability in terms of discrete dipoles, both electronic and ionic, following Sec. II C. Electronic dipoles are primarily associated to bonds, while ionic dipoles are more easily related to atoms. To treat both kind of dipoles on an equal footing, we introduced Si-centered polarizable units based on the first-neighbor shell.

We assigned all the Wannier functions pertaining to a given Si atom to the polarizable unit centered on that atom. The polarizability of such a unit is then obtained by adding up the individual polarizabilities of its component Wannier functions (Sec. II C 1). Care was taken to account for Wannier functions shared among different units, such as Si-Si bonds and nonbonding O orbitals, with the proper weight of 1/2.

The polarizabilities obtained in this way are shown in Fig. 8 for the two model Si-SiO₂ interfaces. Again, we find that the Si and SiO₂ bulk behavior is recovered within a distance of a few angstroms from the interface, in accord with the analysis in Sec. V B. Notice that the outermost Si layers show a polarizability close to the value of the inner layers, while a bump is observed in the local permittivity profile (Fig. 6). In our discrete formulation, the contribution leading to the bump is concentrated in the polarizable units belonging to the suboxide region (see Appendix B). The inset of Fig. 8 shows that there is a monotonic relation between the oxidation state of the central Si atom in the polarizable unit and the corresponding polarizability.

The lattice contribution to the dielectric screening is here evaluated as described in Sec. II C 2. As a reference, we first determined the transverse Born charges for bulk SiO₂, obtaining $Z_{\text{xx, Si}}^B=3.30$ and $Z_{\text{xx, O}}^B=1.65$ for Si and O atoms, respectively. These values agree well with previous calculations for crystalline⁴⁵ and amorphous SiO₂.⁴⁶ Figure 9 shows the calculated effective charges ζ_{xx} across our model Si-SiO₂ interfaces. The effective charges correctly reproduce

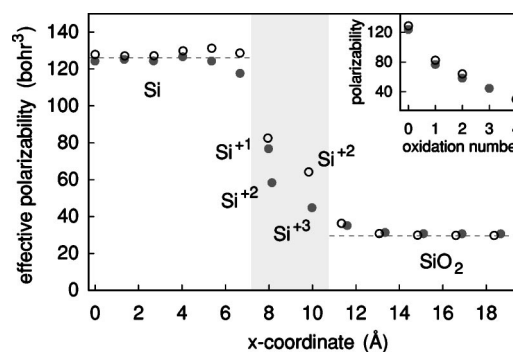


FIG. 8. Effective electronic polarizabilities of Si-centered polarizable units, for model I (disks) and model II (circles) of the Si(100)-SiO₂ interface. The x axis is oriented along the [100] direction. Horizontal dashed lines indicate the values calculated for the corresponding bulk materials. The shaded area indicates the suboxide region. Inset: effective electronic polarizability vs the oxidation state of the central Si atom in the polarizable unit, for both models I (disks) and II (circles).

the reference values obtained for bulk SiO₂ in the stoichiometric oxide, and vanish in the silicon substrate except for the outermost layer. The inset shows a monotonic increase of the effective charges with the Si oxidation state.

The calculated effective charges ζ_{xx} were used to determine the effective ionic polarizabilities through Eq. (26). Figure 10 shows the calculated effective ionic polarizabilities pertaining to the polarizable units defined above for models I and II. Inside the silicon slab, these polarizabilities vanish due to the vanishing effective charges. Within the oxide, the polarizabilities coincide with the values determined for the corresponding bulk. For the polarizable units adjacent to the suboxide region, both on the Si and SiO₂ sides of the interface, we observe only slight departures from the bulk values. In the inset, we give the polarizability of the polarizable units as a function of the oxidation state of the central Si atom. Disregarding momentarily the value for the Si⁺² oxidation state in model II, the polarizability vs oxidation state shows a

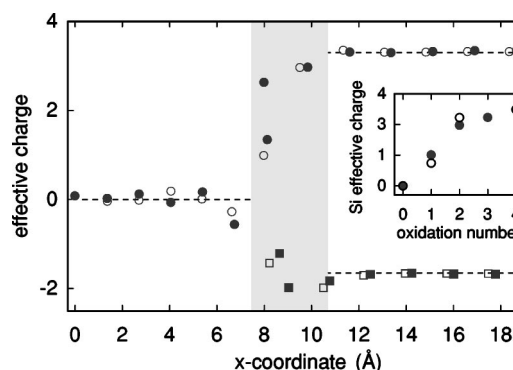


FIG. 9. Effective charges $\zeta_{\text{I,xx}}$ for model I (open symbols) and model II (filled) of the Si(100)-SiO₂ interface. Circles correspond to Si atoms, squares to O atoms. The x axis is oriented along the [100] direction. Horizontal lines indicate the values of the Born dynamical charges calculated for each bulk material separately. Inset: Si effective charges vs Si oxidation state for both model I (disks) and model II (circles).

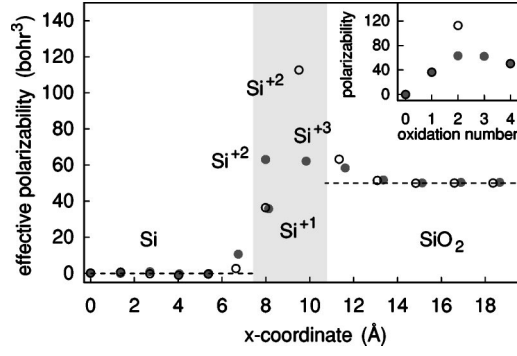


FIG. 10. Effective ionic polarizabilities of the Si-centered polarizable units, for model I (disks) and model II (circles) of the Si(100)-SiO₂ interface. The x axis is oriented along the [100] direction. Horizontal dashed lines indicate the values calculated separately for the corresponding bulk materials. The shaded area indicates the suboxide region. Inset: effective ionic polarizability vs Si oxidation state, for both models I (disks) and II (circles).

rather smooth behavior with a maximum in correspondence with the Si⁺² oxidation state. This result is in accord with the enhanced static permittivity recorded in the suboxide region (Fig. 6). The higher polarizability value found for the Si⁺² oxidation state in model II is related to the occurrence of a Si-Si bond with a bond length of 2.66 Å, considerably larger than the bond length of 2.35 Å found for the corresponding Si⁺² polarizable unit in model I.

Overall, the analysis in terms of discrete polarizabilities conveys the same picture as the local permittivity profile. In addition, this analysis highlights the relation between the dielectric transition across the Si-SiO₂ interface and the chemical grading.⁹

VI. CONCLUSION

In this work, we develop a theory for investigating at the atomic scale permittivity profiles across interfaces between insulators. An expression for the local permittivity is derived from the microscopic induced polarization. We show that the permittivity can conveniently be analyzed in terms of maximally localized Wannier functions. In this way, variations of the local permittivity can be associated to specific features of the bonding arrangement, such as elongated bonds, first-neighbor shells, etc.

In our theory, difficulties in treating the nonlocality of the microscopic susceptibility tensor $\chi_{ij}(\mathbf{r}, \mathbf{r}'; \omega)$ are overcome by focusing on a strictly local quantity $\chi(x; \omega)$, which is diagonal in real space. This is achieved at the cost of restricting our description to length scales which are of the order of interatomic distances. We generally found that such a local description is meaningful for length scales exceeding the spread of the maximally localized Wannier functions.

We illustrated the potential of our scheme by considering two applications of practical relevance. For Si slabs of finite size, our approach indicates that the decrease of the permittivity with slab thickness is related to surface rather than volume effects. The local permittivity in the slab interior was found to be independent of slab size beyond a critical thick-

ness of 13 Si MLs, suggesting that the quantum confinement of the electrons has a negligible effect on the permittivity of the inner layers.

Our scheme for the local permittivity was then applied to the Si-SiO₂ interface. Using two different interface models, we found that the dielectric transition from Si to SiO₂ is rather abrupt, occurring over a width of a few angstroms. We found that the effective polarizability associated to intermediate oxidation states of Si is enhanced with respect to the bulk oxide, leading to a larger permittivity of the interfacial suboxide layer.

In this work, we provided a description of the variation of the local permittivity along a given direction. After taking averages in the orthogonal planes, we critically relied on Eq. (6) for deriving the microscopic polarization from the induced charge density in a gauge-invariant way. The definition of a local dielectric permittivity varying in three dimensions constitutes a desirable extension of the present scheme. However, in this case, Eq. (6) alone is no longer sufficient for determining the microscopic polarization, which remains undetermined by a divergence-free component. While the induced local polarization can in principle be calculated through the transient induced current,¹¹ the computational effort becomes significantly more demanding.

Nonetheless, it should be noted that a truly three-dimensional description remains easily accessible through the effective polarizabilities defined in Sec. II C. Indeed, these polarizabilities are well defined also in the three-dimensional case through the sole knowledge of the induced dipoles and the effective electric field, without requiring the microscopic polarization. A description in terms of such polarizabilities can be highly effective in identifying the dielectric response of specific structural units.

ACKNOWLEDGEMENTS

The calculations were performed at the central computational facilities of the Ecole Polytechnique Fédérale de Lausanne (EPFL) and at Swiss Center for Scientific Computing (CSCS).

APPENDIX A: NONLOCALITY AND WANNIER FUNCTION SPREAD

In this appendix, we relate the typical decay length of the homogeneous real-space dielectric function⁴⁷ to the spread of the maximally localized Wannier functions. To this end, we sequentially make use of expressions relating the decay length to the dielectric constant, the dielectric constant to the band gap, and finally the band gap to the Wannier spread.

Within the Thomas-Fermi approximation, the homogeneous dielectric function in Fourier space can be expressed as⁴⁷

$$\varepsilon(k) = 1 + \frac{\varepsilon_m - \sin(kR)/(kR)}{\sin(kR)/(kR) + (\lambda k)^2}, \quad (\text{A1})$$

where R is the screening radius,⁴⁷ $\varepsilon_m \equiv \varepsilon(k=0)$ is the macroscopic dielectric permittivity, and

$$\lambda^2 \equiv \frac{\pi^2 \hbar^2 \epsilon_m}{4\pi e^2 m k_F}, \quad (\text{A2})$$

with k_F indicating the valence Fermi momentum, and m the electron mass. Instead of Eq. (A1), we here consider an approximate expression for $\epsilon(k)$,

$$\epsilon(k) \approx 1 + \frac{\epsilon_m - 1}{1 + (\lambda k)^2}, \quad (\text{A3})$$

which leaves its shape essentially unchanged and retains the correct limiting behavior at both small and large k . For the parameters adopted in Ref. 47, corresponding to silicon, germanium, and diamond, respectively, we checked numerically that the dielectric functions obtained by using Eqs. (A1) and (A3) differ by at most 20% over the full range of k . The Fourier transform of the $\epsilon(k)$ defined by Eq. (A3) is obtained analytically and gives the nonlocal dielectric function

$$\epsilon(|\mathbf{r} - \mathbf{r}'|) = \delta(|\mathbf{r} - \mathbf{r}'|) + \frac{\epsilon_m - 1}{4\pi\lambda^3} \frac{\exp(-|\mathbf{r} - \mathbf{r}'|/\lambda)}{|\mathbf{r} - \mathbf{r}'|/\lambda}, \quad (\text{A4})$$

where $\delta(|\mathbf{r} - \mathbf{r}'|)$ indicates a Dirac delta normalized to unity. Equation (A4) clearly defines a decay length λ for the extent of nonlocality effects in the dielectric function.

The dielectric permittivity ϵ_m can be related to the optical properties of the system through the Penn model⁴⁸

$$\epsilon_m = 1 + \left(\frac{\hbar\omega_p}{E_p} \right)^2, \quad (\text{A5})$$

where E_p is the Penn gap⁴⁹ and ω_p is the plasma frequency of the electrons

$$\omega_p^2 = \frac{4\pi e^2}{3\pi^2 m} k_F^3. \quad (\text{A6})$$

Since we are interested in estimating order of magnitudes, we replace E_p with the direct band gap E_g and neglect the first term on the right-hand side of Eq. (A5), obtaining

$$\epsilon_m \approx \left(\frac{\hbar\omega_p}{E_g} \right)^2. \quad (\text{A7})$$

Finally, it has been shown that there exists a relation between the direct band gap and the spread ξ of the Wannier functions maximally localized along a given direction^{13,50}

$$\xi^2 < \frac{\hbar^2}{2mE_g}. \quad (\text{A8})$$

By combining the equations above, we obtain the relation

$$\lambda r_0 > (2\pi\sqrt{3})^{1/3} \xi^2 \approx 2\xi^2, \quad (\text{A9})$$

where r_0 corresponds to the radius of the sphere occupied on average by one electron and constitutes a measure of the valence electron density. This equation provides a relation between the decay length of nonlocality effects λ and the Wannier spread ξ . When $r_0 \sim \xi$, as is the case in the systems considered in this work, relation (A9) indicates that a local description of the dielectric properties can only be achieved

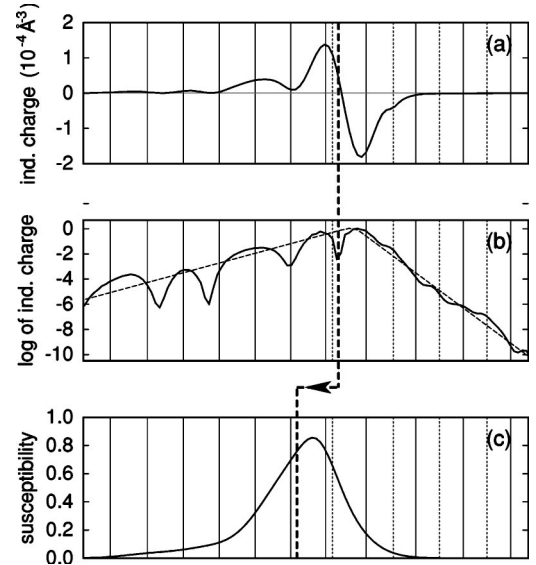


FIG. 11. (a) Induced charge density corresponding to a $\text{Si}^{1+}\text{-Si}^{2+}$ bond in the suboxide of model II of the $\text{Si}(100)\text{-SiO}_2$ interface. The magnitude of the electric field applied to the simulation cell is 10^{-3} a.u. The vertical bold line indicates the center of the Wannier function. (b) Same as (a) but in absolute value and on a logarithmic scale (solid). We also show the corresponding approximation in terms of decaying exponentials (dashed). (c) Contribution to the susceptibility profile arising from the same bond as in (a), (b). The bold dashed line indicates the center of the distribution, clearly shifted towards the Si slab. In all panels, vertical lines represent planes of Si (solid) and O (dotted) atoms.

on length scales which exceed the Wannier spread ξ .

APPENDIX B: ASYMMETRIC DIPOLE DENSITIES AT THE Si-SiO₂ INTERFACE

We investigated the enhancement of the permittivity observed at the edge of the silicon region of the Si-SiO₂ interface (Sec. V B) by means of the Wannier function approach introduced in Sec. II B.

Focusing on interface model II, where the effect is more prominent, we distinguished the contributions to the susceptibility arising from Si-Si bonds in the Si slab and from Si-Si bonds in the suboxide (Fig. 7). We only address Si-Si bonds since Si-O bonds and nonbonding O orbitals were found to be far less polarizable so that their effect is negligible in this context. As shown in Fig. 7, the origin of the enhancement clearly results from the contribution due to the Si-Si bonds in the suboxide. Notice that this contribution peaks within the Si slab, although the suboxide Si-Si bonds from which it originates are located outside the Si slab.

To clarify this point, we focus on a $\text{Si}^{1+}\text{-Si}^{2+}$ bond of the suboxide. We show in Fig. 11 that the corresponding charge density induced by a positive electric field decays exponentially away from the center of the bond, with two different decay lengths in Si and SiO₂: $\lambda_{\text{Si}} \approx 1.7$ Å and $\lambda_{\text{SiO}_2} \approx 0.7$ Å. By means of a simple model, we show in the following that such different decay lengths give rise to an asymmetric contribution to the local susceptibility, which peaks in the Si slab.

We assume a sharp interface at $x=0$ between a dielectric of permittivity ϵ_l on the left and one of permittivity ϵ_r on the right. Following Fig. 11, we model the induced charge density of a single Wannier function as

$$\rho_{\text{ind}}(x) = \begin{cases} -\rho_{\text{ind}}^l \exp(x/\lambda_l) & x < 0, \\ \rho_{\text{ind}}^r \exp(-x/\lambda_r) & x > 0, \end{cases} \quad (\text{B1})$$

where ρ_{ind}^l and ρ_{ind}^r are coefficients which satisfy the condition of charge neutrality

$$\rho_{\text{ind}}^l \lambda_l = \rho_{\text{ind}}^r \lambda_r. \quad (\text{B2})$$

Using Eqs. (13)–(17), we derive the contribution $\delta\chi(x)$ of this Wannier function to the local susceptibility

$$\delta\chi(x) \propto \begin{cases} \epsilon_l \exp(x/\lambda_l), & x < 0, \\ \epsilon_r \exp(-x/\lambda_r), & x > 0. \end{cases} \quad (\text{B3})$$

The mean of this distribution is found to be

$$\langle x \rangle = \frac{\epsilon_r \lambda_r^2 - \epsilon_l \lambda_l^2}{\epsilon_r \lambda_r + \epsilon_l \lambda_l} \approx -\lambda_l, \quad (\text{B4})$$

where the last equality holds when $\epsilon_r \lambda_r \ll \epsilon_l \lambda_l$, as is the case at the Si-SiO₂ interface. Equation (B4) indicates that, while the Wannier function is centered at $x=0$, its contribution to the susceptibility is shifted towards the left by an amount of λ_l . For the Si¹⁺-Si²⁺ bond in the suboxide of model II, Eq. (B4) gives a shift of the susceptibility distribution of about $-\lambda_{\text{Si}} \approx -1.7$ Å, which compares favorably with the shift of -1.62 Å calculated for the actual contribution to the local susceptibility of this bond [Fig. 11(c)].

These considerations show that the origin of the asymmetric susceptibility distribution results from the different decay lengths of the induced charge at the interface. The decay length towards the Si side of the interface is characteristic of bulk Si, while the decay length towards the SiO₂ side results from the evanescent nature of the involved Si states in SiO₂. Indeed, we calculated a typical decay length of mid-gap evanescent states in the oxide of about 0.8 Å, close to the decay length of the induced charge density of the Si-Si bond in SiO₂ ($\lambda_{\text{SiO}_2} \approx 0.7$ Å).

APPENDIX C: REAL-SPACE AVERAGE WITH GAUSSIAN KERNEL

In this appendix, we establish the connection between the averaging procedure through a Gaussian kernel and the well-known macroscopic average.⁵¹ For this purpose, consider an ideal superlattice of period L along the stacking direction, resulting from the alternation of two crystalline slabs with different lattice spacings $b_1 > b_2$, both much shorter than L .

The prescription of the macroscopic average technique consists in filtering twice the function of interest by means of a rectangle kernel.⁵² In reciprocal space this corresponds to applying a weight

$$w(G) = \frac{\sin(Gb_1/2)}{Gb_1/2} \frac{\sin(Gb_2/2)}{Gb_2/2} \quad (\text{C1})$$

to the coefficients in the Fourier expansion. This results in setting equal to zero all the Fourier coefficients which correspond to G 's which are integer multiples of $2\pi/b_1$ or $2\pi/b_2$, without affecting in a significant way the behavior of the function on the scale of the superlattice periodicity since $2\pi/L \ll 2\pi/b_{1,2}$. This method is best suited for a superlattice composed of ideal crystalline slabs. However, when the crystals deviate from perfect periodicity, for instance, in the presence of strain at the interfaces, the method is less efficient in filtering the spurious lattice spacings. Moreover, the extension of this technique to disordered three-dimensional systems with short-range order is not well defined.

We considered a generalization of the macroscopic average which overcomes these shortcomings. To this end, we determined the asymptotic form of the averaging kernel resulting from the serial application of rectangle filters with b_1, b_2, \dots, b_N widths. In reciprocal space, the averaging kernel has the following weight function

$$w_N(G) = \prod_{n=1}^N \frac{\sin(Gb_n/2)}{Gb_n/2}, \quad (\text{C2})$$

which, to lowest order in powers of G , corresponds to

$$\tilde{w}_N(G) \approx \exp(-G^2 \sigma_N^2/2), \quad (\text{C3})$$

where $\sigma_N = \bar{b} \sqrt{N/12}$, \bar{b} being the root mean square period in the series. More generally, the Gaussian weight in Eq. (C3) corresponds to the asymptotic form of Eq. (C2) in the limit of large N , as can be seen by invoking the central limit theorem of probability theory.⁵³

The difference between the rectangle and Gaussian filter resides in the fact that the former sets the coefficients of the frequencies which are multiples of $2\pi/b_n$ exactly to zero, while the latter only suppresses their amplitudes. The larger the width of the Gaussian kernel, the more effective will be this suppression. A compromise must therefore be found between the width of the kernel in real space and the degree of suppression of the undesired Fourier components. For the range of applications considered in this work, we found that the Gaussian filter reduces the amplitudes of the fluctuations to less than 1% of the average value when the full width at half maximum of the real-space kernel is $\sim 1.5 \max(b_1, b_2)$, only slightly larger than the width of the trapezoidal filter corresponding to a double macroscopic average.⁵²

- ¹L.-W. Wang and A. Zunger, Phys. Rev. Lett. **73**, 1039 (1994).
- ²M. Lannoo, C. Delerue, and G. Allan, Phys. Rev. Lett. **74**, 3415 (1995).
- ³C. Delerue, M. Lannoo, and G. Allan, Phys. Rev. B **68**, 115411 (2003).
- ⁴D. E. Aspnes and J. B. Theeten, Phys. Rev. Lett. **43**, 1046 (1979).
- ⁵B. Brar, G. D. Wilk, and A. C. Seabaugh, Appl. Phys. Lett. **69**, 2728 (1996).
- ⁶G. D. Wilk, R. M. Wallace, and J. M. Anthony, Appl. Phys. Lett. **89**, 5243 (2001).
- ⁷*The Dielectric Function of Condensed Systems*, edited by L. V. Keldysh, D. A. Kirzhnits, and A. A. Maradudin (North-Holland, Amsterdam, 1989).
- ⁸R. Resta and A. Baldereschi, Phys. Rev. B **23**, 6615 (1981).
- ⁹F. Giustino, P. Umari, and A. Pasquarello, Phys. Rev. Lett. **91**, 267601 (2003).
- ¹⁰L. L. Hirst, Rev. Mod. Phys. **69**, 607 (1997).
- ¹¹P. Umari, A. Dal Corso, and R. Resta, in *Proceedings of the 11th Williamsburg Workshop on Fundamental Physics of Ferroelectrics* (APS, Williamsburg, 2001), Vol. 582, p. 107.
- ¹²N. Marzari and D. Vanderbilt, Phys. Rev. B **56**, 12 847 (1997).
- ¹³C. Sgarovello, M. Peressi, and R. Resta, Phys. Rev. B **64**, 115202 (2001).
- ¹⁴G. Nenciu, Rev. Mod. Phys. **63**, 91 (1991).
- ¹⁵R. W. Nunes and D. Vanderbilt, Phys. Rev. Lett. **73**, 712 (1994).
- ¹⁶I. Souza, J. Iñiguez, and D. Vanderbilt, Phys. Rev. Lett. **89**, 117602 (2002).
- ¹⁷R. D. King-Smith and D. Vanderbilt, Phys. Rev. B **47**, 1651 (1993).
- ¹⁸X. Gonze and C. Lee, Phys. Rev. B **55**, 10 355 (1997).
- ¹⁹A. A. Maradudin, E. W. Montroll, G. H. Weiss, and I. P. Ipatova, in *Solid State Physics: Advances in Research and Applications*, edited by H. E. Ehrenreich, F. Seitz, and D. Turnbull (Academic, New York, 1971), Suppl. 3, Chap. 4.
- ²⁰J. P. Perdew and Y. Wang, Phys. Rev. B **46**, 12 947 (1992).
- ²¹A. Pasquarello, K. Laasonen, R. Car, C. Lee, and D. Vanderbilt, Phys. Rev. Lett. **69**, 1982 (1992); K. Laasonen, A. Pasquarello, R. Car, C. Lee, and D. Vanderbilt, Phys. Rev. B **47**, 10 142 (1993).
- ²²A. Dal Corso, A. Pasquarello, A. Baldereschi, and R. Car, Phys. Rev. B **53**, 1180 (1996).
- ²³D. Vanderbilt, Phys. Rev. B **41**, 7892 (1990).
- ²⁴R. Car and M. Parrinello, Phys. Rev. Lett. **55**, 2471 (1985).
- ²⁵P. Umari and A. Pasquarello, Phys. Rev. Lett. **89**, 157602 (2002).
- ²⁶R. Resta, *Ferroelectrics* **136**, 51 (1992); R. Resta, Rev. Mod. Phys. **66**, 899 (1994).
- ²⁷F. Gygi, J.-L. Fattebert, and E. Schwegler, Comput. Phys. Commun. **155**, 1 (2003).
- ²⁸R. Resta and S. Sorella, Phys. Rev. Lett. **82**, 370 (1999).
- ²⁹P. Umari and A. Pasquarello, Phys. Rev. B **68**, 085114 (2003).
- ³⁰A. Dal Corso, S. Baroni, and R. Resta, Phys. Rev. B **49**, 5323 (1994).
- ³¹P. Carrier, L. J. Lewis, and M. W. C. Dharma-Wardana, Phys. Rev. B **64**, 195330 (2001).
- ³²Z. H. Lu, D. J. Lockwood, and J.-M. Baribeau, Nature (London) **378**, 258 (1995).
- ³³R. Tsu, D. Babić, and L. Ioriatti, Jr., J. Appl. Phys. **82**, 1327 (1997).
- ³⁴B. K. Agrawal and S. Agrawal, Appl. Phys. Lett. **77**, 3039 (2000).
- ³⁵A. Pasquarello, M. S. Hybertsen, and R. Car, Phys. Rev. B **53**, 10942 (1996); Appl. Surf. Sci. **104**, 317 (1996).
- ³⁶N. Tit and M. W. C. Dharma-Wardana, J. Appl. Phys. **86**, 387 (1999).
- ³⁷F. Rochet, Ch. Poncey, G. Dufour, H. Roulet, C. Guillot, and F. Sirotti, J. Non-Cryst. Solids **216**, 148 (1997).
- ³⁸J. H. Oh, H. W. Yeom, Y. Hagimoto, K. Ono, M. Oshima, N. Hirashita, M. Nywa, A. Toriumi, and A. Kakizaki, Phys. Rev. B **63**, 205310 (2001).
- ³⁹A. Bongiorno and A. Pasquarello, Phys. Rev. B **62**, R16 326 (2000).
- ⁴⁰A. Bongiorno and A. Pasquarello, Appl. Phys. Lett. **83**, 1417 (2003).
- ⁴¹K. Hirose, H. Kitahara, and T. Hattori, Phys. Rev. B **67**, 195313 (2003).
- ⁴²F. Giustino, P. Umari, and A. Pasquarello, Microelectron. Eng. **72**, 300 (2004).
- ⁴³While the size dependence of the position operator introduces an error of 13% on the permittivity of the Si region, the corresponding errors for the suboxide and the oxide regions are smaller than 3%, as we estimated by applying a sawtooth-shaped potential to a SiO₂-Si-SiO₂ slab with oxide surfaces terminated by H atoms.
- ⁴⁴C. M. Perkins, B. B. Triplett, P. C. McIntyre, K. C. Saraswat, S. Haukka, and M. Tuominen, Appl. Phys. Lett. **78**, 2357 (2001), and references therein.
- ⁴⁵X. Gonze, D. C. Allan, and M. P. Teter, Phys. Rev. Lett. **68**, 3603 (1992).
- ⁴⁶A. Pasquarello and R. Car, Phys. Rev. Lett. **79**, 1766 (1997).
- ⁴⁷R. Resta, Phys. Rev. B **16**, 2717 (1977).
- ⁴⁸D. R. Penn, Phys. Rev. **128**, 2093 (1962).
- ⁴⁹S. H. Wemple and M. Di Domenico, Jr., Phys. Rev. B **3**, 1338 (1971).
- ⁵⁰I. Souza, T. Wilkens, and R. M. Martin, Phys. Rev. B **62**, 1666 (2000).
- ⁵¹A. Baldereschi, S. Baroni, and R. Resta, Phys. Rev. Lett. **61**, 734 (1988).
- ⁵²L. Colombo, R. Resta, and S. Baroni, Phys. Rev. B **44**, 5572 (1991).
- ⁵³C. M. Grinstead and J. L. Snell, *Introduction to Probability* (American Mathematical Society, Providence, RI, 1997).